ARTICLE   OPEN

Check for updates

High sensitivity and broad linearity range pressure sensor based on hierarchical in-situ filling porous structure

Jin Xu[1,6], Huayang Li [ID][1,2,6 ✉], Yiming Yin[1], Xin Li[3], Jinwei Cao[1,2], Hanfang Feng[1], Wandi Bao[4], Hao Tan[1], Fanyuan Xiao[5] and Guang Zhu [ID][1 ✉]

Flexible piezoresistive pressure sensor with high sensitivity over a broad linearity range have been attracting tremendous attention for its applications in health monitoring, artificial intelligence, and human-machine interfaces. Herein, we report a hierarchical in-situ filling porous piezoresistive sensor (HPPS) by direct ink writing (DIW) printing and curing of carbon nanofibers (CNFs)/ polydimethylsiloxane (PDMS) emulsion. Hierarchical geometry significantly increases the contact area, distributes stress to multilayered lattice and internal porous structure, resulting in a broad sensing range. Moreover, unlike conventional hollow porous structure, the CNFs networks in-situ filling porous structure generates more contact sites and conductive pathways during compression, thereby achieving high sensitivity and linearity over entire sensing range. Therefore, the optimized HPPS achieves high sensitivity (4.7 kPa^{-1}) and linearity (coefficient of determination, $R^2 = 0.998$) over a broad range (0.03–1000 kPa), together with remarkable response time and repeatability. Furthermore, the applications in diverse pressure scenarios and healthcare monitoring are demonstrated.

INTRODUCTION

Flexible pressure sensors with the capacity of transducing tactile information into electric signals have attract huge attention because of their promising applications in health monitoring[1–5], artificial intelligence[6,7], human-machine interfaces[8–10], robotics[11,12], etc. Typically, flexible pressure sensors are categorized into four types based on the sensing mechanism: piezoresistvie[13,14], capacitive[15,16], piezoelectric[17,18] and triboelectric[19,20]. Among these pressure sensors, piezoresistive sensors which transfer the mechanical information into resistance variation, has multiple advantages including low energy consumption, ease of device assembly, and simple signal acquisition, etc. However, most published piezoresistive pressure sensors suffer from low sensitivity or poor linearity over a broad range. To widespread deployment of the pressure sensors in more application scenarios, the ideal pressure sensors require high sensitivity and high linearity over a broad sensing range.

Recently, several strategies to enhance the sensitivity and linearity have been reported. Preparation of nanostructure or microstructure geometries (such as wrinkles[21], micropyramids[22], microdomes[23], micropillars[24], interlock structure[25], etc.[26,27]) on the flexible substrate can significantly enhance the sensitivity due to the low initial current and large deformability under low stress. For example, Tao et al.[28] reported an interlocking microdome-structured based piezoresistive pressure sensor with a high sensitivity of 53 kPa^{-1} and the pressure range from 58.4 to 960 Pa. Whereas the rapidly saturated microstructure contacts sites during compression results in the high sensitivity and linear response only valid in a low sensing range (<10 kPa). To extend the linear sensing range, the introduction of porous structure has been proved an effective way because of the high compressibility

and considerable conductive pathways generation during compression. Seunghwan et al.[29] developed a porous sponge sensor with the sensitivity of 0.01–0.02 kPa^{-1} under broad sensing range from 10 Pa to 1.2 MPa. Nevertheless, the pores increase the distance among the conductive fillers which hinder the contact of conductive fillers and generation of conductive pathways. Thus, most of the porous pressure sensors exhibit a low sensitivity (<1 kPa^{-1}) over a broad range. A few studies proposed the multi-layer or multiscale hierarchical structure with enhancement in both sensitivity and linear sensing range. For instance, Youngoh Lee et al.[30] fabricated a tactile sensor with multilayer interlocked microdome geometry which presented high sensitivity of 47.7 kPa^{-1} over the range from 0.0013 to 353 kPa. However, the linear sensing range of the sensors are still not sufficient. Therefore, there is strong needed to fabricate a high performance (e.g., a linear response with high sensitivity over 1 kPa^{-1} over the range up to 1 MPa) pressure sensor in a simple and cost-effective way.

Herein, we propose a hierarchical in-situ filling porous structure as the sensing layer fabricated by DIW printing and curing of CNFs/PDMS emulsion. The hierarchal geometry increases the variation of contact area and distributes the applied stress to multilayered lattice structure and internal porous structure. A Face-Centered Tetragonal (FCT) structure is designed with the highest compressibility compared with other types of lattice structures, enabling a broad sensing range and high sensitivity.

The CNFs in-situ filling porous structure has a very different morphology and working principles from the conventional porous structure, which led to the better sensing performance of the in-situ filling porous structure. For conventional porous structures fabricated by hard templates or gas foaming method[29], the

[1]New Materials Institute, Department of Mechanical, Materials and Manufacturing Engineering, University of Nottingham Ningbo China, 315100 Ningbo, China. [2]CAS Key Laboratory of Magnetic Materials and Devices, Ningbo Institute of Materials Technology and Engineering, Chinese Academy of Sciences, 315201 Ningbo, China. [3]School of Nanoscience and Technology, University of Chinese Academy of Sciences, 100049 Beijing, China. [4]Ningbo Sezen Technology Co., Ltd, 315042 Ningbo, China. [5]College of Mechanical and Electrical Engineering, Beijing University of Chemical Technology, 100029 Beijing, China. [6]These authors contributed equally: Jin Xu, Huayang Li ✉email: huayang.li@nottingham.edu.cn; guang.zhu@nottingham.edu.cn
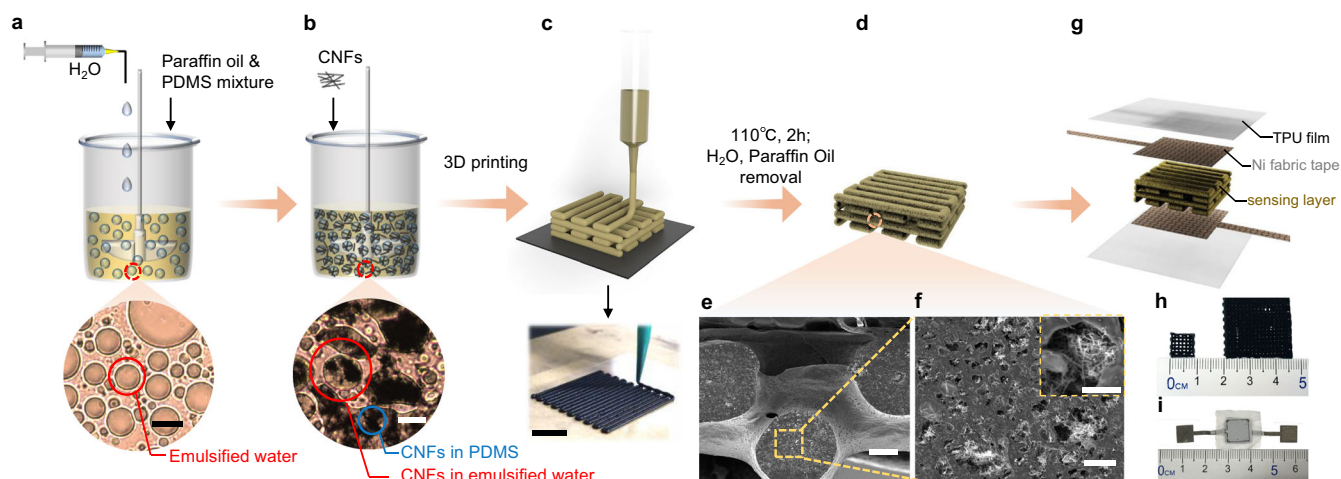
Fig. 1 Overview of the HPPS. Schematic illustration of the fabrication of hierarchical in-situ filling porous structure. Schematic diagram and microscope images of **a** PDMS emulsion, **b** CNFs/PDMS emulsion (scale bar: 20 μm). **c** Schematic diagram and optical image of hierarchical in-situ filling porous structure by DIW printing (scale bar: 1 cm). **d** Schematic diagram of hierarchical in-situ filling porous structure. **e** Cross-sectional SEM image of the multilayered lattice structure (scale bar: 200 μm). **f** Cross-sectional SEM image of inner porous structure in a single lattice rod (scale bar: 200 μm). Inset high magnification SEM image of CNFs networks embedding in a single pore structure (scale bar: 5 μm). **g** Schematic structure of the HPPS. **h** Optical image of hierarchical in-situ filling porous structure with different sizes. **i** Optical image of HPPS.

conductive fillers are separated and excluded by the hard templates or foaming process, resulting in the conductive filler being dispersed only at the edge of the pores. The large space of the pores hinders the contact of the conductive fillers dispersed at the edges of the pores, resulting in fewer conductive paths being generated. The in-situ filling porous structure is formed by the solidification of CNFs/PDMS and evaporation of emulsified water, while the CNFs dispersed in emulsified water remain inside the pores, forming CNFs networks embedded in the pores. The CNFs networks in-situ filling in porous structure dramatically increases the conductive material contact sites and conductive pathways generation during compression, which achieves high sensitivity and high linearity.

Based on such a hierarchical geometry and secondary CNFs in-situ filling porous structure, the HPPS achieves a high sensitivity (4.7 kPa^{-1}) and high linearity ($R^2 = 0.998$) over a broad range (0.03–1000 kPa) simultaneously. The high sensitivity and linearity enable the pressure sensor with a high-pressure resolution. Therefore, the sensor is capable of detecting a low-pressure change (10 kPa) under a high pre-compression of 643 kPa. The HPPS are used in detecting various stimuli from low pressure such as pulse detection, voice recognition, to large pressure such as human foot motion, tire pressure detection. The demonstration of slight pressure changes upon large pre-compression indicated our pressure sensors have a high-pressure resolution. In addition, a smart insole sensor array comprising of 5 sensors located in different positions is employed for plantar pressure sensing to diagnose foot diseases and detection of sports biomechanics. With the remarkable sensing performance, we envisage that the hierarchical in-situ filling porous structure can provide a promising design strategy to fabricate high-performance wearable devices for applications in health monitoring, artificial intelligence, human-machine interfaces, robotics, etc.[11,12]

RESULTS

Fabrication and structural characterization of HPPS

The fabrication process of the hierarchical in-situ filling porous structure by DIW printing technique are illustrated in Fig. 1. First, the PDMS emulsion was prepared by adding the aqueous solution with the calcium chloride concentration of 3.5 wt% dropwise into PDMS/Paraffin liquid mixture through syringe pump (Fig. 1a). After vigorous mechanical stirring, the emulsified water droplets are uniformly distributed in the mixture to form creamy PDMS-water emulsion, which is shown in the optical microscope images in Fig. 1a. Second, the CNFs were added into the PDMS emulsion. Because of the mobilities and containable properties of the emulsified water, the added CNFs can disperse in the emulsified water, PDMS matrix and PDMS-water interfaces as presented in Fig. 1b. The photograph of the PDMS emulsion and CNFs/PDMS-emulsion are presented in Supplementary Fig. 1a and b, respectively. Furthermore, the CNFs/PDMS emulsion with high shear thinning behavior and large storage modulus is beneficial in extruding and preserve self-standing 3D lattice structure as interpreted in Supplementary Fig. 2a and b, respectively. Thus, the CNFs/PDMS emulsion can be extruded uniformly and continuously from the nozzle and stacked layer-by-layer to construct 3D lattice structure (Fig. 1c). Moreover, the samples with different 3D lattice structures can be continuously printed by the DIW technique (in Supplementary Fig. 3). Then, the printed CNFs/PDMS emulsion lattice structure is heated at 110 °C to make the PDMS fully cure, and emulsified water evaporate, which results in the formation of hierarchical in-situ filling porous structure with the CNFs networks embedded in the internal porous, as shown in Fig. 1d. The cured CNFs/PDMS lattice structure needs to be washed twice in n-Hexane and ethanol, respectively, and subsequently dried at 110 °C for 2 h to remove the paraffin oil to prevent the degradation of sensing performance. (Supplementary Fig. 4). After the Paraffin is removed, the hierarchical in-situ filling porous layer is well prepared. Meanwhile, the prepared porous layer shows good bending capacity (Supplementary Fig. 5). The Scanning Electronic Microscopy (SEM) image of the rod in lattice structure is shown in Supplementary Fig. 6a. As the emulsified water embedded with the CNFs evaporates, the CNFs networks is left in the internal pores, which can be seen in the cross-sectional SEM images of the rod (Fig.1e,f). Figure 1e shows the cross-sectional view of the hierarchical in-situ filling porous sensing layer consist of multilayers of lattice rods with a distance of approximately 500 μm between each rod. On the cross-sectional surface of a single lattice rod (Fig. 1f), the internal porous structure with the diameter of 5–10 μm evenly distribute in the lattice rod. The small gap of around 1 μm among the embedded CNFs networks is observed in a single pore structure (Inset images
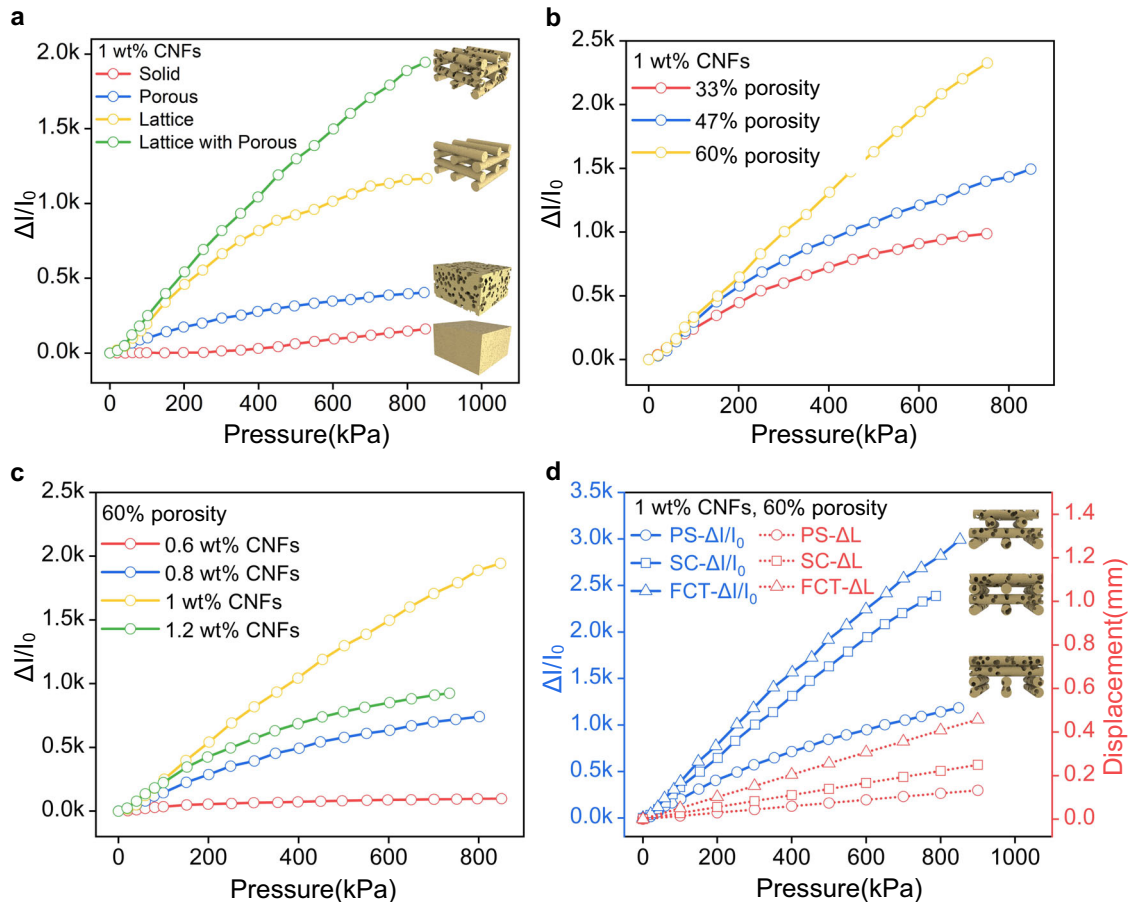
Fig. 2 Current response and sensitivity of HPPS with different parameters of sensing layer. a Current response and sensitivity of 1 wt% CNFs, 60% porosity pressure sensor with different geometrical structures (solid, porous, lattice, lattice with porous). Current response and sensitivity of four layers SC pressure sensor with different mass ratio of **b** water (**c**) CNFs. **d** Current response and sensitivity of 1 wt% CNFs, 60% porosity pressure sensor with different lattice structures (PS, SC and FCT).

of Fig. 1f). In addition, the SEM image in Supplementary Fig. 6b, shows that some CNFs networks also exist in the PDMS matrix. With the advantages of DIW technique, the custom fabricated lattice structures with different sizes (1×1 cm^2 and 2.5×2.5 cm^2) are shown in Fig. 1h, respectively. The schematic diagram of the whole assembled HPPS is shown in Fig. 1g, in which the hierarchical in-situ filling porous structure serving as the sensing layer and the Ni fabric tape (Supplementary Fig. 7) and thermoplastic polyurethanes (TPU) electrospinning film (Supplementary Fig. 8) act as the electrodes and protective layers, respectively. The optical image of the assembled HPPS is shown in Fig. 1i.
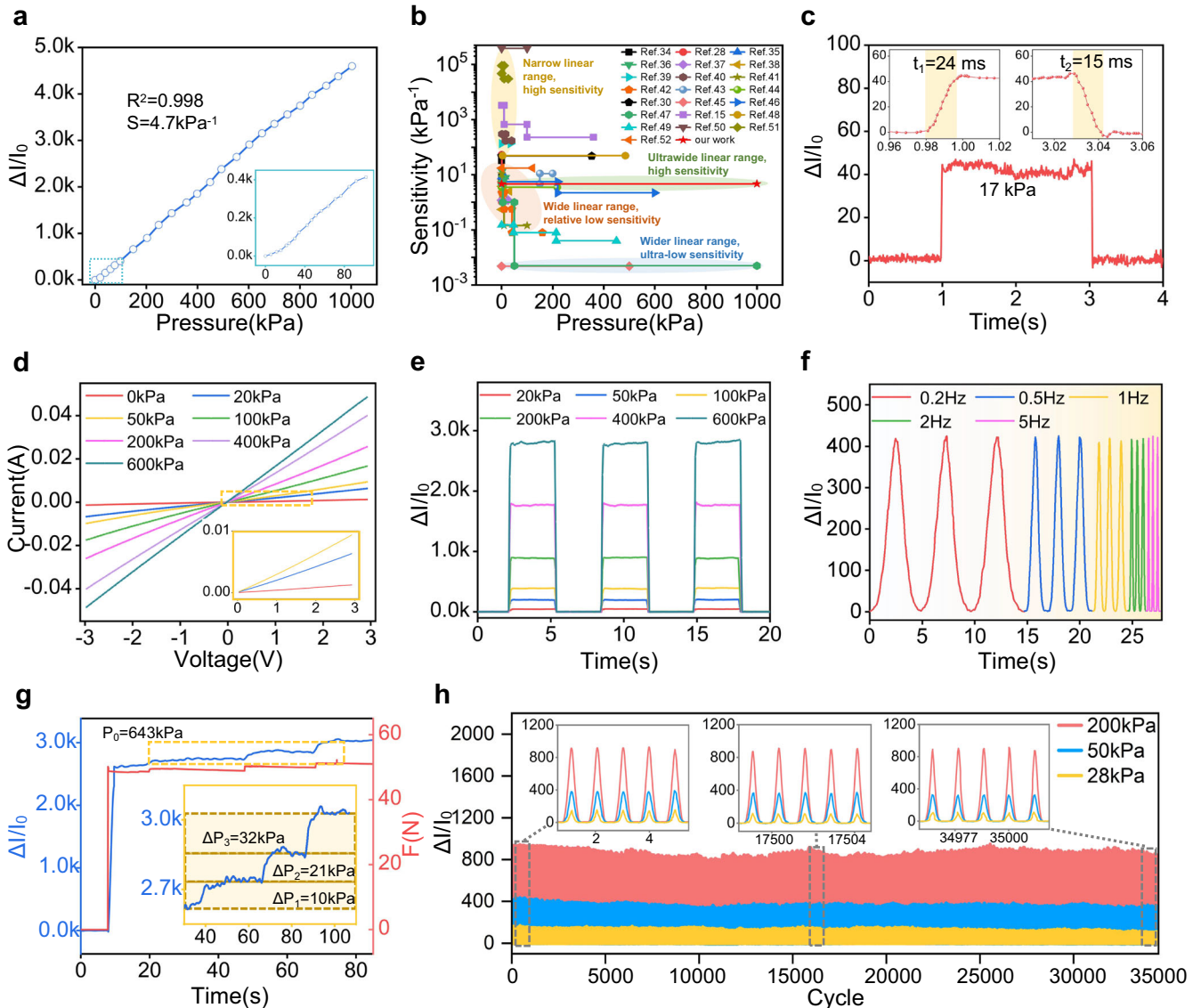
Parameter optimization of the sensing layer in HPPS

To develop the optimal preparation parameters for the sensing layer, the influence of the porosity, CNFs mass ratio, structure types and stacked sensing layer numbers are thoroughly investigated, respectively. Here, when one of the variables is studied, the other ones remain unchanged. And the pressure sensitivity (S) is defined as $S = (\Delta I/I_0)/\Delta P$, where ΔI represents the current change of the sensor, I_0 represents the current without pressure and ΔP represents the applied pressure. The experiment setup for detecting the current change of the sensor is schematically shown in Supplementary Fig. 9.

First, four kinds of sensing layers with the same extended contour volume were prepared and investigated, as depicted in Fig. 2a, Supplementary Fig. 10, Supplementary Fig. 11 and Supplementary Table 1. The solid structure has the lowest

sensitivity of 0.19 kPa^{-1}, while the porous structure and the lattice structure have higher sensitivity of 0.47 kPa^{-1} and 1.65 kPa^{-1}, respectively. As we all know, a higher compression generates more conductive pathways within the sensing layers. So, the porous structure formed by emulsion template method has higher compressibility under the same pressure. For lattice structure, the macroscale gap between the lattice rods produced by DIW also provides higher compressibility. Here, the synergetic effect of the internal porous and lattice structure endows the structure with the highest compressibility among them, which results in the highest sensitivity of 2.4 kPa^{-1} with high linearity ($R^2 = 0.993$). Note that for the effect of composition of water and CNFs, and structure types, the layer numbers are fixed at four because the structures with four layers possess the best sensing performance compared with the structures with other layers. The reason of four layer-structure has the best sensing performance is explained in detail in Supplementary Fig. 12, Fig. 13, Fig. 14 and Table 2.

Second, the effect of composition of water on sensing performance is well studied in Fig. 2b. Based on the previous studies and comparative experiments (Supplementary Table 3) about the effect of amounts of emulsified water on porosity, the porosity could be simply adjusted by varying the mass ratio of water in the emulsion system[31,32]. The porosity increases with the increasing content of the emulsified water. The porosity is characterized through mass difference method (see the Experimental Section for details). As shown in Fig. 2b, the higher porosity structure exhibits higher sensitivity. Compared with the sensors with porosity of 33% and 47%, the pressure sensor with 60%

Fig. 3 Evaluation of electromechanical performance of HPPS. a Relative current change based on the optimized sensing layer under different pressures (0.032 kPa–1000 kPa). **b** Comparison of the sensitivity of our pressure sensor with other reported literatures. **c** Response and recovery times of the HPPS under the pressure of 17 kPa. **d** Current-voltage curves of the HPPS under different pressures. **e** Dynamic response of the HPPS under loading/unloading cycles from low pressure to high pressure. **f** Dynamic response of the HPPS under 100 kPa at different frequencies. **g** Detection of tiny pressure under pre-compression of 643 kPa. **h** Repeatability performance of HPPS over 35,000 loading/unloading cycles under the pressure of 28 kPa, 50 kPa, and 200 kPa respectively.

porosity exhibits an improved sensitivity (3.2 kPa^{-1}) and linearity ($R^2 = 0.998$) in the range of 0–750 kPa. This is because the higher porosity structure with the lower young modulus is more compressible under the same pressure. Thus, a subtle pressure would largely deform the structure and create more conductive pathways in the high porosity structure.

Third, the content of CNFs also has an observable effect on the sensors. So, the sensors with the CNFs mass ratio ranging from 0.6 wt% to 1.2 wt% are prepared and its influence on the sensitivity are studied in Fig. 2c. For the sensors prepared with the CNFs amount from 0.6 wt% to 1 wt%, the sensitivity gradually improved. The increased mass ratio of the conductive fillers can construct more conductive pathways when applied with the same pressure, which results in a higher sensitivity. However, excessive CNFs greatly reduce the resistance in the original state (I_0), which leads to a decrease in the relative current changes. As a result, the sensitivity of the sensor with 1.2 wt% CNFs is lower than the sensor with 1 wt% CNFs.

Finally, three different lattice structures: Simple cubic (SC), Parallel Stacked (PS), and FCT[33] are simply fabricated through DIW based on the designed structural model. All the lattice structures are fabricated with the same amount of emulsion. The design diagrams of the SC, PS and FCT structures are shown in Supplementary Fig. 15, respectively. The sensitivities and compression simulation are shown in Fig. 2d. With the optimal content of water and CNFs, the FCT structure exhibits the highest sensitivities among them. Different sensitivity of three lattice structures results from the degree of deformability of the lattice structure. Then, the finite element analysis (FEA) is performed to analyze the deformation and the stress distribution of three lattice structures are shown in Supplementary Figs. 16 and 17 and Video 1, respectively. In the simulation results, the PS structure has the smallest displacement ($\Delta L = 148\,\mu m$), and the FCT structure has the largest displacement ($\Delta L = 508\,\mu m$). The simulation result is consistent with the experiment result. Compare with PS and SC structures, the FCT structure experiences a dominant deformation
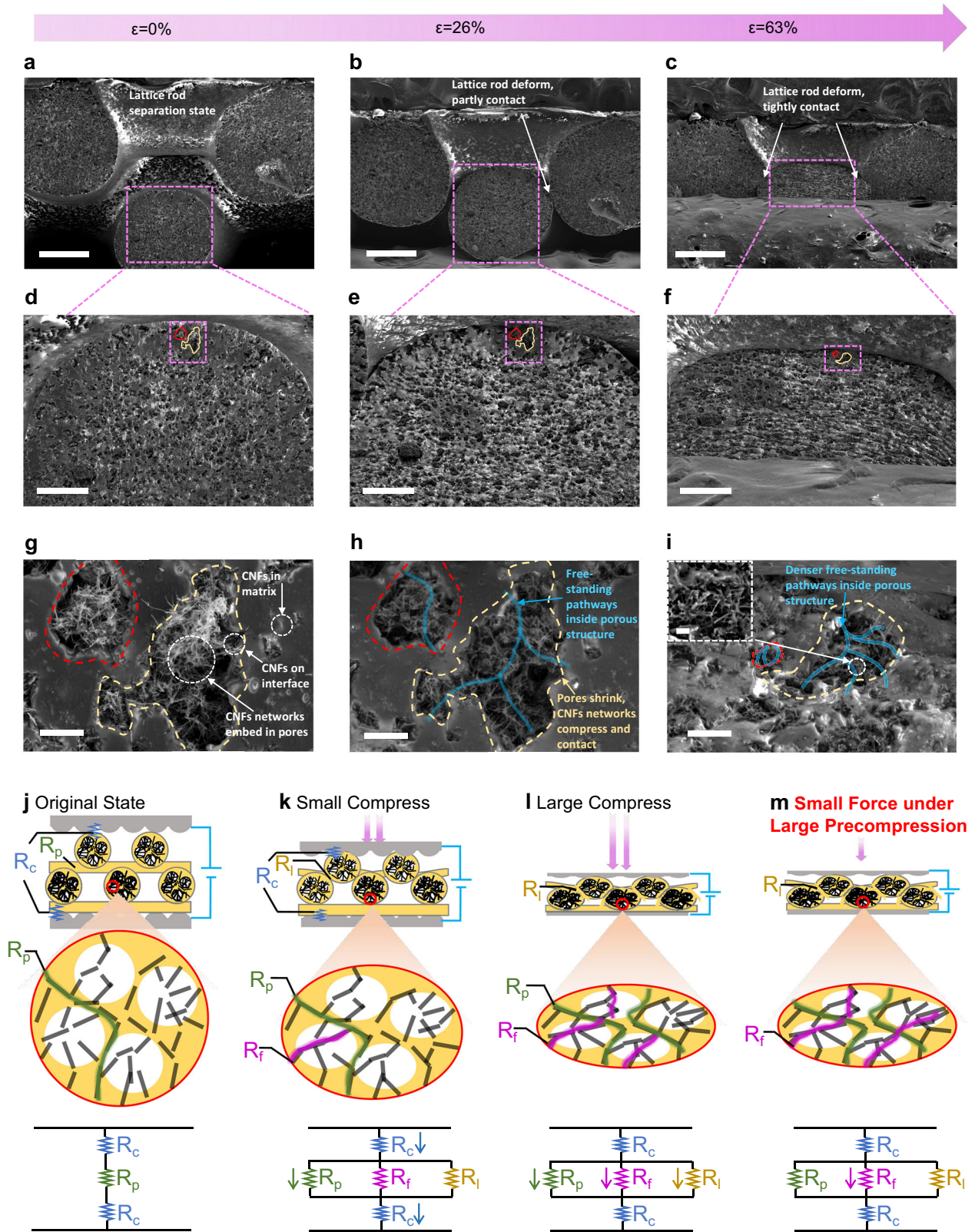
Fig. 4 In-situ SEM images of structural deformation of hierarchical in-situ filling porous structure during compression and schematic description of sensing mechanism. Cross-sectional SEM images of lattice structure at **a** original state, **b** compression of 26%, **c** compression of 63% (scale bar: 300 μm). Cross-sectional SEM images of the porous structure at **d** original state, **e** compression of 26%, **f** compression of 63% (scale bar: 100 μm). Cross-sectional SEM images of the CNFs networks embedding in a single pore at **g** original state, **h** compression of 26%, **i** compression of 63% (scale bar: 10 μm; **i** inset image scale bar: 3 μm). Schematic illustration and circuit diagram of sensing mechanism of HPPS under **j** small compression, **k** medium compression, **l** large compression. **m** A tiny pressure change under a large preload is used to illustrate the high pressure resolution performance.

provided by compressing the staggered rods rather than compress the vertically aligned rods in PS and SC structure. So, the stress is homogeneously distributed in the contact sites of each perpendicular stack layer. In short, based on the above optimization of the HPPS, it is determined that the 60 wt% water, 1 wt% CNFs, four layers and the FCT lattice structure are the optimal preparation conditions.

Sensing performance of HPPS

The sensing performance of the HPPS under different pressing conditions is studied. The synergetic effect of in-situ filling internal porous structure and lattice structure enables the sensor with high sensitivity and high linearity over a broad pressure-sensing range. As shown in Fig. 3a, the HPPS prepared with the optimized condition (1 wt% CNFs, 60 wt% water with FCT structure) achieves a high sensitivity of 4.7 kPa^{-1} and high linearity with the correlation coefficient of 0.998 in the broad pressure ranging from 0.032 to 1000 kPa. In comparison with the previously reported piezoresistive pressure sensors in Fig. 3b[15,28,30,34–52], our HPPS exhibits a high sensitivity and a broad linearity range of pressure. The HPPS exhibit a low detection limitation of 32 Pa as shown in Supplementary Fig. 18. The dynamic response speed of the sensor is measured by suddenly pressing with a 17 kPa force followed by a quick release. The response and relaxation time are 24 ms and 15 ms (Fig. 3c), respectively, which are comparable to the response time of human skin (30–50 ms)[12]. The current-voltage (I–V) curves of the pressure sensor from −3 V to 3 V under different pressures display a linear relationship, indicating that the HPPS possesses the Ohmic contact characteristics (Fig. 3d). As the pressure increases from 0 to 600 kPa, the resistance decreases dramatically. The relative current change of sensor under six incremental pressure loading/unloading cycles is measured to investigate the dynamic pressure sensing performance (Fig. 3e). The pressure sensor exhibits a steady signal and transient response to the cyclic loading/unloading process, indicating that the pressure sensor is capable of working stably in a wide range. The effect of loading frequency should also be considered for evaluating the stability of dynamic pressure sensing performance. As depicted in Fig. 3f, the relative current change exhibits no frequency dependence or delay under constant pressure of 100 kPa with frequency from 0.2 to 5 Hz. The high sensitivity and high linearity under a broad pressure range enable the pressure sensor with high-pressure resolution. The pressure sensor could detect the slight pressure change under a high pre-compression. Figure 3g depicts the synchronous change of current and pressure. At first, the sensor is compressed to 643 kPa as the reference P_0, and then the incremental slight pressure (10 kPa, 21 kPa, and 32 kPa) were added in sequence. The results show that the sensor has the ability to differentiate the incremental slight press under a large pre-compression. As illustrated in Fig. 3h, the pressure sensor exhibits high reproducibility and durability under the pressure of 28 kPa, 50 kPa and 200 kPa during 35,000 cycles, respectively. In the inset figure, the signal shows that there is no obvious amplitude change in the cycle test. To study the reproducibility of the pressure sensor, the error bar studies in terms of pressure range and sensitivity were conducted by measuring eight sensors in Supplementary Fig. 19 and Supplementary Table 4. All eight sensors have very close sensitivity values over a wide sensing range of 1 MPa. Furthermore, all eight sensors exhibit very high linearity. There is no significant deviation in sensitivity and linearity, which implies the good reproducibility of the pressure sensor.

The sensing mechanism of HPPS

The synergic effect of multilayer structure and hierarchical in-situ filling porous structure enables the pressure sensor with high sensitivity, high linearity over a broad pressure range. In order to understand the high-performance sensing mechanisms of HPPS, micromechanics compression test and in-situ SEM imaging are performed. For all the following SEM images, the compression direction is vertical (up to down). Figure 4a–i visualizes the cross-sectional views of structure evolution at 0%, 26%, and 63% compression at different scales. The schematic illustration of the detailed sensing mechanism is depicted in Fig. 4j–m and Supplementary Fig. 20.

Supplementary Fig. 21 visualizes the interface between the sensing layer and the Ni electrodes. The wavy textile micro-structure of Ni electrodes forms fewer initial contact points with the sensing layer, which results in high contact resistance in the unloaded state. Figure 4a, d, g and j illustrate the morphology of multilayer lattice and hierarchical in-situ filling porous structure before compression. The space between stacked layers makes the lattice structure highly compressible (Fig. 4a). The in-situ filling porous structure formed by emulsion template method results in CNFs networks exists in PDMS matrix, on the interface, and embedded in pores (Fig. 4d and g). This could create more contact sites among CNFs networks during compression, resulting in a high sensitivity over the sensing range.

At very low compression (Supplementary Fig. 21), the contact area (orange line) between the Ni electrodes and sensing layer increases significantly, resulting in a decrease in contact resistance under low pressure range. In addition, the internal pores compress slightly, and CNFs networks embedded in porous structure slightly contact each other, generating some conductive pathways that increase the current. A comparison experiment (Supplementary Fig. 22) of the effects of wavy textile microstructure electrode and flat Cu electrode on the sensing performance under low pressure is conducted to prove that the Ni electrodes can improve the sensing performance in low pressure range. Furthermore, there is no significant deviation in sensitivity between the low pressure (4.64 kPa^{-1}, <500 Pa) and high pressure range (4.7 kPa^{-1}, <1 MPa), which further confirms the high sensitivity and linearity over the entire sensing range.

At 26% compression (Fig. 4b, e, h and k), the lattice rods deform and partly contact with each other to create more conductive pathways. Comparing with the single-layer structure, the multi-layer structure has a larger contact area change and effective stress distribution, thereby generating more conductive pathways during compression[30,53]. This is also verified in sensitivity test of different layers in Supplementary Fig. 12. In the high magnifications SEM images of Fig. 4e and h, inner pores (red dash line, yellow dash line) begin to shrink, and CNFs networks embedded in porous structure contact each other to build up more conductive pathways. The introduction of in-situ filling porous structure further improves the sensitivity and linearity. This can be proved by the results in Fig. 2a, where the sensitivity of lattice structure with internal porous structure is higher than the lattice structure without it.

Herein, a schematic illustration of Supplementary Fig. 20, is used to interpret the high-performance mechanism of in-situ filling porous structure compared with other kinds of conventional hollow porous structure. The superiority of our in-situ filling porous structure to conventional porous structures is caused by different morphologies and different working principles. For the conventional porous structures which are usually fabricated by hard templates (like sugar, salt, and other solid particle templates) or gas foaming method, the conductive fillers are separated and excluded by the hard templates or foaming process. This results in the conductive filler can only be dispersed at the edge of the pores. When

applied with a slight pressure change, the large space of the pores hinders the contact of conductive fillers dispersed at the edge of the pores, which results in most conductive paths generating only in the elastomer. Therefore, for conventional porous sensors, the resistance change is relatively small over the entire sensing range. For our in-situ filling porous structure fabricated by soft emulsion template method, the CNFs can disperse inside the soft template when mixed with PDMS emulsion. Then, during the high temperature curing process, the emulsified water evaporates, while the CNFs dispersed in emulsified water remain inside the pores, forming CNFs networks embedded in the pores. This led to the conductive fillers not only attaching at the edge of the pores but also in-situ filling in the pores. When a slight pressure change is applied, the CNFs networks embedded in internal porous

structure can easily contact each other to generate free-standing conductive pathways in the internal pores. In addition, the CNFs networks also could serve as a 'bridge' to connect the separated conductive filler dispersed at the edges of the pores to form more conductive pathways. This result in the conductive path could generate in elastomer, pores, and elastomer-pores interface. Therefore, a more significant resistance change can be induced over the entire sensing range. A comparison of sensing performance of the in-situ filling porous sensor with conventional porous sensor with the same porosity and same ratio of CNFs is conducted to further prove the superiority of in-situ filling porous structure to conventional porous structure (Supplementary Fig. 23).

At 63% compression (Fig. 4c, f, i and l), the further deformation and tight contact of lattice rods will generate more conductive
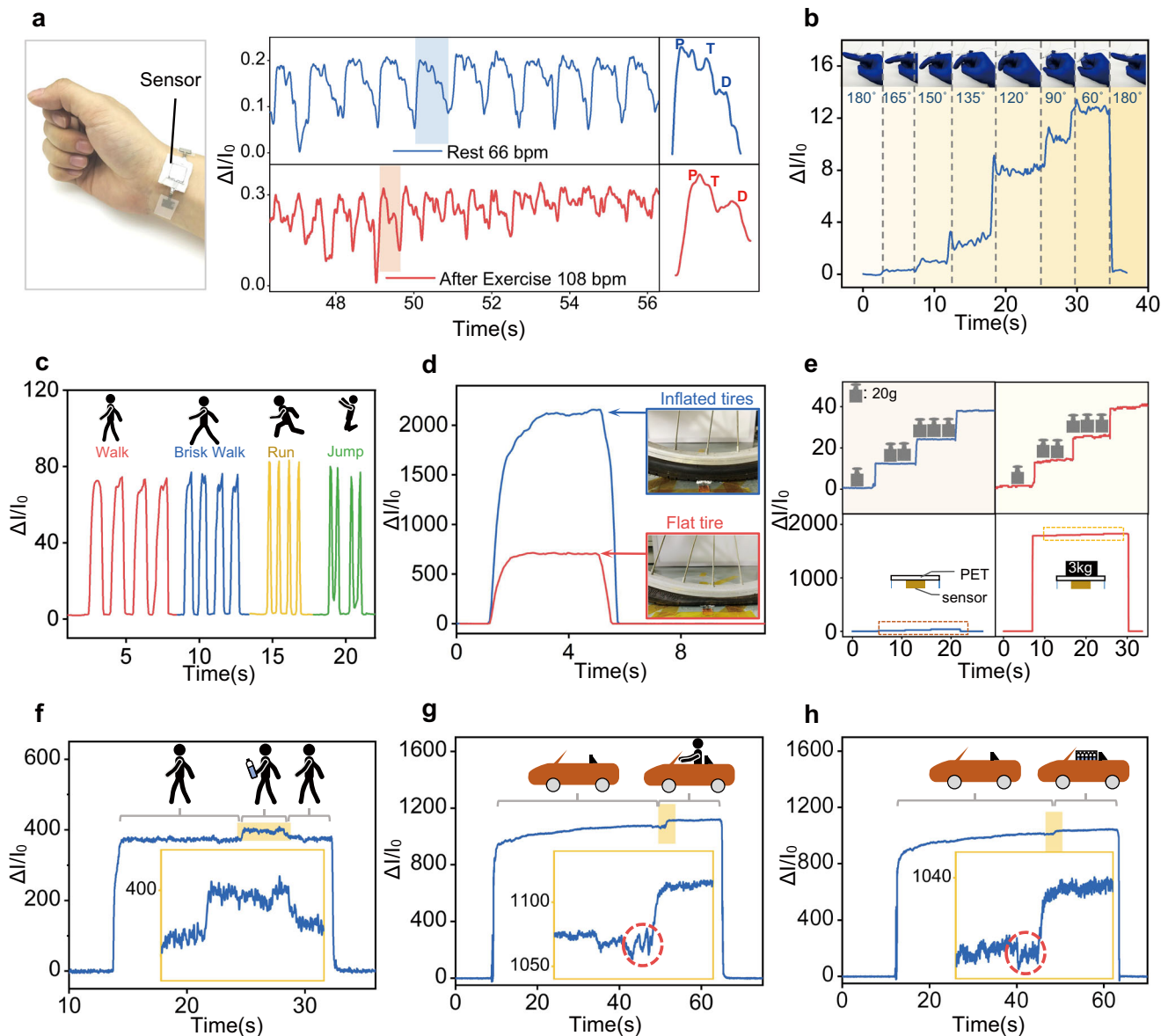
Fig. 5 Applications of HPPS in real-time monitoring of human activities, detection of small physical signals and demonstrations of high-sensing resolution. a HPPS attached to the wrist to monitor the wrist pulse of a healthy person before and after exercise, and the enlarged single pulse signal contains characteristic peaks: P-wave, T-wave, and D-wave. **b** Monitoring of finger bending with different angles. **c** Real-time recording of the human motions including walking, brisk walking, running and jumping. **d** Measuring the tire pressure while riding a bicycle. **e** Measuring the three 20 g weight changes in sequence under the pre-loading weights of 0 and 3 kg. **f** Measuring the tiny pressure change of a bottle of water under the preload of a human weight. Measuring the pressure change of **g** a human and **h** a box of water under the preload of a car weight.
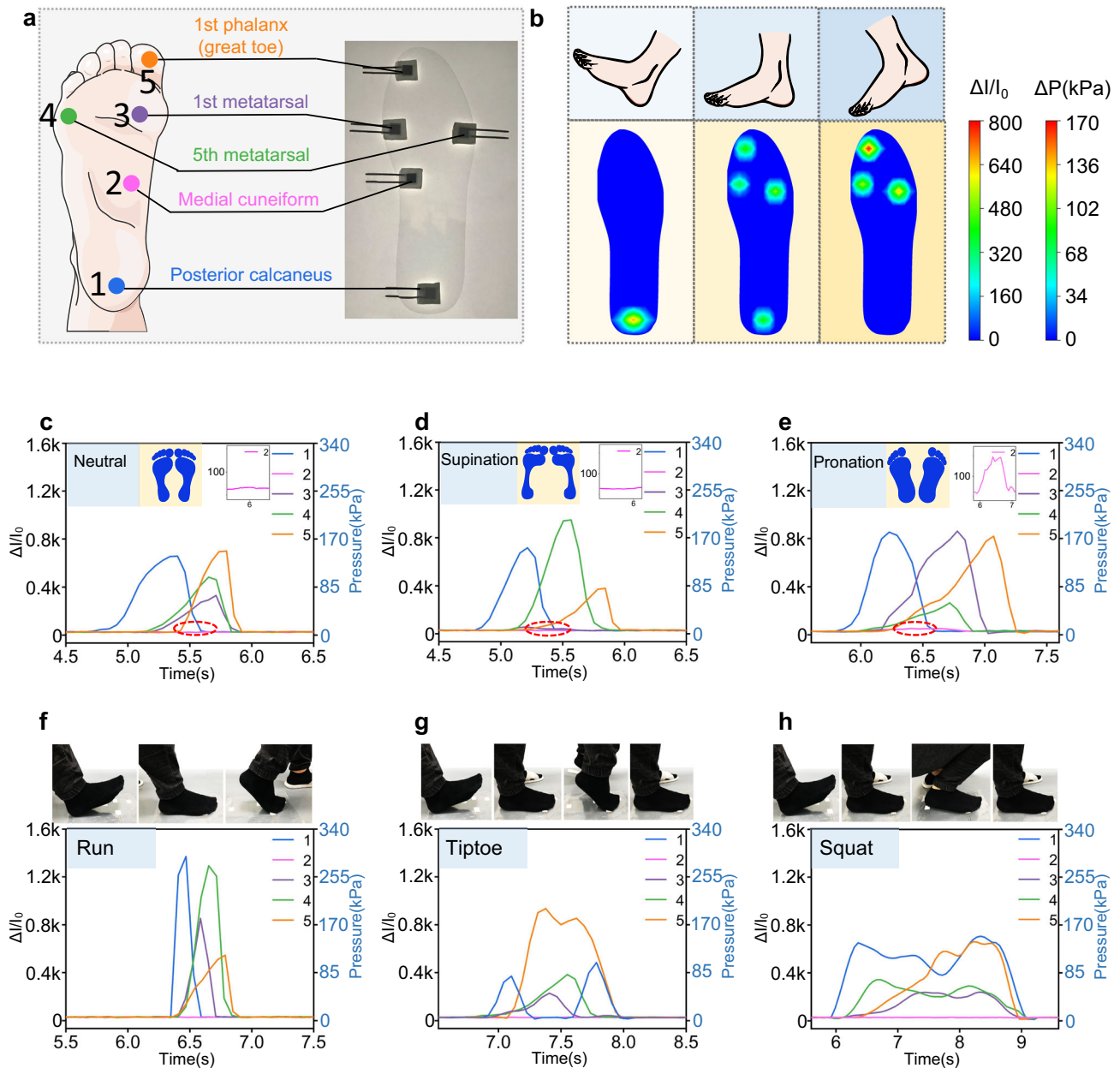
Fig. 6 Flexible smart insole composed with HPPS array for plantar pressure monitoring. a Optical image of HPPS array on smart insole and correspond anatomy in the schematic illustration of human foot. **b** Evolution of the pressure distribution mapping during dynamic waking process. Real-time recorded current variations and corresponding calculated pressure of the five sensors to detect walking posture of three different people with (**c**) Neutral gait (**d**) Supination gait (**e**) Pronation gait, respectively. Real-time recorded current variations and corresponding calculated pressure of the five sensors to recognize sports biomechanics of (**f**) Running (**g**) Standing on tiptoe (**h**) Squatting, respectively.

pathways and reduce resistance. In the high magnifications SEM images of Fig. 4f and i, the pores further shrink, and the CNFs networks embedded in porous structure compressed to form more conductive pathways. During the entire process of compression, conductive pathways are generated continuously due to the gradual contact of in-situ filling CNFs networks in microscale and deformation and contact of lattice rods in macroscale.

It can be observed from Fig. 4i and m, even at a highly compressed of 63%, there are still some nano-scale gaps between each carbon nanofiber due to the mesh characteristics of the CNFs networks. Thus, upon a huge pre-compression, a slight pressure change could still induce some conductive pathways to generate

in nanoscale CNFs networks. This can be demonstrated by the result in Fig. 3g.

The total resistance of HPPS is expressed in terms of the sum of the resistance of the sensing material (R_p, R_f) and contact resistance (R_c, R_l). In theory, the total resistance is expressed as follows Eq. (1):

$$R_{total} = 2R_c + \frac{R_p * R_f * R_l}{R_p * R_f + R_p * R_l + R_f * R_l} \tag{1}$$

where R_c denotes the contact resistance between the sensing layer and the electrode, R_l denotes the contact resistance between the neighboring interlocked lattice rod, R_p denotes the resistance of the conductive pathways generate in PDMS matrix and R_f

denotes the resistance of the free-standing pathways generate inside the porous structure.

Wearable device and high-pressure resolution demonstration

Due to the high sensitivity and high linearity over a broad range, the pressure sensor can be used in various applications. As present in Supplementary Fig. 24, different slight pressure is detected and distinguished to verify the high sensitivity and high-pressure resolution of the HPPS. In order to detect the slight pressure, adhesive tape is used to fix the sensor tightly on the table. The light objects' weight from a grain of rice (0.022 g) to a tiny screw (0.7 g) are detected and distinguished based on the difference of the current change. Due to its high sensitivity, the sensor can be used to detect the wrist pulse period and waveform in real-time when it is attached to the wrist skin by the medical tape (Fig. 5a). As illustrated in Fig. 5a, the arterial pulse could be read out accurately under both normal conditions (66 beats per minute) and after exercise (108 beats per minute). Meanwhile, each periodic pulse with three distinguishable characteristic peaks can be accurately recognized in both states: percussion wave (P), tidal wave (T), and diastolic wave (D). This suggests that the HPPS could potentially apply in healthcare monitoring and disease diagnosis. Next, the pressure sensor is used to recognize different voices (Supplementary Fig. 25). As shown in the inset, the sensor is attached on the throat to detect the subtle vibration when the volunteer speaks. The words 'Good' and 'morning' correspond to characteristics of current change pattern, indicating that the sensor is capable of distinguishing different voices. The word 'good' is repeated five times to demonstrate its repeatability. In addition, the angle of finger bending could also be accurately measured (Fig. 5b, Supplementary Fig. 26, and Video 2). When the bending angle of the finger gradually changes, the current change exhibits a stepwise increase. The current change remains constant when the finger maintains a certain angle, and it returns to the original value when the finger restores to the original position. As shown in Fig. 5c and Supplementary Video 3, the pressure sensor is fixed on the sole to detect the different motion states. Different motions including walking, brisk walking, running, and jumping could be distinguished according to the sharpness, frequency, and intensity of the signal in Fig. 5c. Sensor can be utilized to measure tire pressure during riding a bicycle, as shown in Fig. 5d. When riding a bicycle with inflated tires, the tires generate large pressure on the sensor, which results in a large current signal. When the tire is out of air, the contact area of the tire with the ground becomes larger, resulting in a decrease in the pressure of the tire on the sensor. Sensors with a wide range can potentially be applied to tactile perception of human-machine interfaces to detect small pressures such as blowing, touching, and then larger pressures such as stabbing and smashing (Supplementary Fig. 27). Moreover, the pressure sensor is used as an electronic balance to verify the linear sensitivity at high pressure, as depicted in Fig. 5e. The square PET plate is placed on top of the sensor to bear the weight, and four small columns are located at four corners to stabilize the PET. When three incremental weights (20 g, 40 g, 60 g) were sequentially loaded under 0 kg and 3 kg pre-loading weights, the current changes for each 20 g mass increase in both cases exhibit the same value, indicating the good linearity of the pressure sensor under high pressure.

Above all, the HPPS has a great potential in detecting the incremental small press under a large pre-compression. In Fig. 5f–h, a $2.5 \times 2.5\ cm^2$ pressure sensor is used to demonstrate the high-pressure resolution characteristics under a broad pressure range. As shown in Fig. 5f, an 80 kg male stands with one foot on the pressure sensor and then a bottle of water (~550 g) was placed on his hand. The whole process, including the slight pressure change due to the addition a bottle of water, can be detected by the current change. Moreover, in another experiment (Fig. 5g and Supplementary Video 4), the front wheel of a car (1700 kg) is first pressed on the sensor as pre-compression. When a male (80 kg) is getting on the car, the increased pressure leads to a stepped raise of the current change. When the car leaves the pressure sensor, the signal instantly recovers to its original state. As shown in Fig. 5h and Supplementary Video 5, a lighter object (a box of bottled water, 6 kg) is placed on the car. The entire process, including the weight change of a box of bottled water, could be accurately recorded through the obvious signal change. The signal oscillations (marked in red circle) in inset of Fig. 5g, h indicate the slight vibration and movement while a man and a box of water loaded on the car.

Plantar pressure distribution monitoring

Plantar pressure distribution monitoring is of great significance in podiatric diseases prevention and diagnosis, injury prevention, gait analysis, and sports biomechanics, etc[30,54]. For instance, abnormal gait and walking posture may cause excessive local pressure in certain areas of the foot, which can lead to various diseases such as, plantar fasciitis, diabetic foot ulcers, etc[55,56]. The typical abnormal gait including supination and pronation is shown in inset images in Fig. 6d, e. Except for congenital supination and pronation, some acquired cases result from wearing unfit shoes, being overweight, or calcium deficiency or poor walk habits. For the acquired supination and pronation, it is difficult to prevent and diagnose the disease at an early stage[57].

Herein, our highly sensitive over broad range pressure sensor is capable of accurately detecting plantar pressure distribution, which can be used to diagnose abnormal gait at an early stage. The high linearity of pressure sensor is able to clearly distinguish the pressure intensity of different local areas. As schemed in Fig. 6a, five pressure sensors are integrated into the smart insole. Each sensor is placed at corresponding areas of posterior calcaneus (#1), medial cuneiform (#2), 1st metatarsal (#3), 5th metatarsal (#4) and 1st phalanx (#5). The evolution of pressure distribution map during dynamic waking process (heel strike, mid stance and toe-off) is reconstructed from the acquired signals, as shown in Fig. 6b.

Figure 6c–e demonstrate and compare the current variation and corresponding calculated pressure as a function of time for three different walking gaits: neutral, supination and pronation. For neutral gait (Fig. 6c), the #1 sensor signal increases first due to the heel touches the ground. Then the #3,4 sensor signal rise indicates the mid stance, and finally, the #5 sensor signal growth suggests that the heel lift in the final stage. For supination gait (Fig. 6d), the signal of sensor #4 is much higher than sensor #3 which indicates a shift of barycenter to the outside of the foot (5th metatarsal). In the case of pronation (Fig. 6e), the shifting of barycenter to the inside of the foot leads to a higher signal in sensor #3 (1st metatarsal). In addition, the early stage of pronation gait results in a slightly flat foot, which causes the arch slightly to deform to touch the #2 sensor (medial cuneiform) as shown in the inset image in Fig. 6e. Therefore, the high sensitivity of the pressure sensor enables to identification of minor gait abnormalities, thereby realize diagnose of pronation and supination in the early stage. The high linearity of the pressure sensor could easily distinguish three different walking gaits by comparing the plantar pressure distribution.

In addition to prevention and diagnosis of foot diseases, our sensor can also be applied to sports biomechanics detection (Fig. 6f–h). Compare with normal walking (Fig. 6c, step speed: 48 steps per minute), a larger current signal and higher frequency are observed during running (Fig. 6f, step speed: 100 steps per minute). During the process of standing on tiptoe (Fig. 6g), more pressure is concentrated on 1st phalanx, which causes an intense signal in sensor #1. During the squatting process (Fig. 6h), the signal experience a constantly changes because of the altering barycenter. The above results indicate that the high sensitivity and high linearity over the broad range pressure sensor have outstanding potential in wearable medical devices and sports equipment for real-time monitoring purposes.

DISCUSSION

In summary, we designed a hierarchical in-situ filling porous pressure sensor with high sensitivity and high linearity over a broad sensing range. The DIW printed hierarchical geometry achieves a broad sensing range because the multilayer lattice and internal porous structure increases contact area and distributes applied stress. The strategy of in-situ formation of CNFs networks embedded inner porous structure provides a significantly and continuously increase in contact area in each single pore, which results in a high sensitivity and high linearity. Therefore, our pressure sensor achieves high sensitivity ($4.7\ kPa^{-1}$) and high linearity ($R^2 = 0.998$) over a broad range (0.03–1000 kPa). These sensing capabilities enable the pressure sensor to detect diverse stimuli from low pressure such as pulse detection, voice recognition, finger binding detection in medium pressure regimes to human foot motion, tire pressure monitoring in high pressure regions. Moreover, the sensor is able to detect a low pressure change under a high compression because of its high-pressure resolution. With the outstanding performance of the pressure sensor, it can be applied to personal electronics and biomedical devices in the near future. In addition, this cost-effect fabrication method of hierarchical in-situ filling porous structure provide a general design strategy for other types of sensors.

METHODS

Materials

Carbon nanofibers (CNFs, model XFM60, purity > 95 wt%) with a diameter of 50–200 nm and a length of 1–15 μm were purchased from XFNANO company. The PDMS matrix (Sylgard 184) and curing agent were bought from Dow Corning Co., Ltd. Paraffin liquid was obtained from Sinopharm Chemical Reagent Co., Ltd. N-hexane (AR, 97%), 1,1,1,3,3,3-Hexafluoro-2-propanol (99.5%), and Ethanol (ACS, purity > 99.5%) were purchased from Aladdin Co., Ltd. TPU pellets were purchased from Bayer Material Science.

Preparation of CNFs/PDMS emulsion as DIW printing ink

The PDMS matrix Sylgard 184 (5 g) and curing agent fully mixed in a ratio of 10:1 in a 50 ml beaker. Then the prepared PDMS solution was diluted with paraffin liquid (5 g) by a high-shear dispersing machine (FS400-S, LICHEN Co., Ltd) at a stirring speed of 1200 rpm. Then the aqueous solution with the calcium chloride concentration of 3.5 wt% was added dropwise by microfluid syringe pump machine (SP-1000, Ningbo Annuo Medical Apparatus, and Instruments Technology Co., Ltd) with a flow rate of 48 ml/h under mechanical stirring. After all the water was added into the PDMS/paraffin liquid mixture, a white and creamy PDMS emulsion was obtained. Then a certain ratio of CNFs was mixed thoroughly to form a black and creamy CNFs/PDMS emulsion ink. Upon the completion of the preparation, the CNFs/PDMS emulsion ink was ready for characterization and DIW printing.

Characterization of CNFs/PDMS emulsion ink (morphology of emulsion; rheological measurement)

The morphology of the PDMS emulsion and CNFs/PDMS emulsion was characterized by upright microscope (ZEISS Axio Imager Vario) with objective lens (40×). The emulsion was dripped on the microscope slide and covered with a coverslip before observation.

Rheological behaviors of inks were obtained using a rheometer (Physica MCR-301, Anton Paar GmbH Co., Ltd) at the ambient temperature (25 °C). The ink shear viscosity was measured by increasing the shear rate from 10^{-2} to $10^{3}\ s^{-1}$. Shear storage modulus(G′) and viscous loss modulus(G″) were obtained in an oscillatory mode with a constant frequency of 1 Hz in the stress range from 10^{-2} to 10^{3} Pa.

CNFs/PDMS emulsion was used as ink, DIW printed lattice structure as pressure sensitive layer

The 3D CNFs/PDMS emulsion lattice structure was fabricated using pneumatic extruding DIW printing (SHOTmini200ΩX, Musashi Engineering, Inc.). All DIW printed lattice structure was fabricated base on the lattice structure models designed by 3D modeling software in DIW printer. The

printed lattice structure was extruded and deposited on the PET substrates. Based on primary optimization, the nozzle diameter was 0.84 mm, the print head moving speed was $6\ mm\ s^{-1}$, and the extrusion pressure was controlled in the range of 50–100 kPa according to various compositions of CNFs/PDMS emulsion. After DIW printing, the CNFs/PDMS emulsion lattice structure was heated in an oven at 110 °C for 2 h to curing while evaporating the emulsified water. The cured CNFs/PDMS lattice structure was washed twice in n-Hexane and ethanol respectively and subsequently dried at 110 °C for 2 h in an oven. The thickness of the CNFs/PDMS lattice structure with four layer is around 1.6 mm.

The porosity of the CNFs/PDMS emulsion lattice structure was controlled by the amount of water added while the ratio of CNFs: PDMS is fixed. The porosity of CNFs/PDMS sponge was calculated based on the following Eq. (2):

$$porosity = \frac{m_{(CNF/PDMS\ block)} - m_{(CNF/PDMS\ sponge)}}{m_{(CNF/PDMS\ block)}} \quad (2)$$

Preparation of the HPPS

The fabrication of HPPS was as follows: First, the TPU film as the encapsulation layer was prepared by electrospinning of 4 wt% TPU dissolved in 1,1,1,3,3,3-Hexafluoro-2-propanol with a positive voltage of 10 kV and a negative voltage of 2 kV. The TPU film was cut into $2 \times 2\ cm^2$ for protective layer. The pattern of the electrode was design using CorelDRAW software. A laser cutting machine (4060, FST) was used to engrave the conductive fabric tape to the predesigned pattern. Then the two pieces of cut conductive fabric tapes transferred to the two pieces of cut TPU film as the top electrode and bottom electrode, respectively. The sensing layer of HPPS was encapsulated between two pieces of square TPU film with the conductive fabric tape.

Structural characterization and electromechanical performance of the sensors

The morphology and microstructure of the samples were observed by Field emission scanning electron microscopy with the voltage of 5 kV (Sirion200, FEI, USA). The computer-controlled linear motor (LinMot) and a digital force gauge (Mark-10, USA) were used to provide and measure the pressure, respectively. Two pieces of PMMA square plate with a length of 1 cm long and a thickness of 1 mm were stick on the head of digital force gauge and the head of the linear motor, respectively. The sensor was stick on the PMMA plate on the head of the digital force gauge. For pressure-sensing performance, the linear motor was set to apply pressure according to appropriate testing conditions. The pressure was recorded by the digital force gauge. Meanwhile, the current was recorded in real-time using a LabVIEW controlled digital source meter (Keithley 2611B). The source-drain voltage was 0.1 V, except for the high-pressure resolution demonstration (Fig. 3g) was 0.07 V. The I–V curves were measured by an electrochemical analyzer (CHI660E) in the pressure range of (0–600 kPa). For the high-pressure resolution test (Fig. 3g), tiny object pressure sensing test (Supplementary Fig. 24), pulse detection (Fig. 5a), voice recognition (Supplementary Fig. 25), high-pressure resolution demonstration (Fig. 5f–h), the current was recorded using an electrometer (Keithley 6514).

The $3 \times 3\ cm^2$ sensor was used for high-pressure resolution demonstration (Fig. 5f–h), and the $1 \times 1\ cm^2$ sensor was used for all other tests and demonstrations. The sensitivity (S) was calculated according to the following Eq. (3):

Sensitivity(S)

$$S = \frac{\Delta I/I_0}{\Delta P} \text{ or } \frac{\Delta R/R_0}{\Delta P} \quad (3)$$

Where I_0 is the initial current of the sensor without pressure loading, and ΔI is the current changes of the sensor under a fixed pressure change(ΔP).

Finite element analysis simulation

The stress and displacement distribution of PS, SC, and FCT lattice structures under external pressure were simulated by using COMSOL software. The single lattice rod was set as 1 mm long and 0.5 mm in diameter, the distance between two lattice rods was set as 1 mm. Two plates were given the steel properties to sandwich the lattice structure. A linear compressive force was applied to compress the lattice structures.

Fabrication of smart flexible insole

The foot-shaped PET film was cut by laser cutting machine. The 5 pressure sensors lay out on the 5 positions of PET film, including 1st phalanx (#5), 5th metatarsal (#4), 1st metatarsal (#3), Medial cuneiform (#2), and Posterior calcaneus (#1).

DATA AVAILABILITY

The data that support the findings of this study are available from the corresponding author upon reasonable request.

REFERENCES

1. Schwartz, G. et al. Flexible polymer transistors with high pressure sensitivity for application in electronic skin and health monitoring. *Nat. Commun.* **4**, 1859 (2013).
2. Son, D. et al. Multifunctional wearable devices for diagnosis and therapy of movement disorders. *Nat. Nanotechnol.* **9**, 397–404 (2014).
3. Chen, G. et al. Electronic Textiles for Wearable Point-of-Care Systems. *Chem. Rev.* **122**, 3259–3291 (2022).
4. Meng, K. et al. Wearable Pressure Sensors for Pulse Wave Monitoring. *Adv. Mater.* **34**, e2109357 (2022).
5. Libanori, A. et al. Smart textiles for personalized healthcare. *Nat. Electron.* **5**, 142–156 (2022).
6. Rus, D. & Tolley, M. T. Design, fabrication and control of soft robots. *Nature* **521**, 467–475 (2015).
7. Kim, Y. et al. A bioinspired flexible organic artificial afferent nerve. *Science* **360**, 998–1003 (2018).
8. Jung, S. et al. Reverse-micelle-induced porous pressure-sensitive rubber for wearable human-machine interfaces. *Adv. Mater.* **26**, 4825–4830 (2014).
9. Jeong, J. W. et al. Materials and optimized designs for human-machine interfaces via epidermal electronics. *Adv. Mater.* **25**, 6839–6846 (2013).
10. Araromi, O. A. et al. Ultra-sensitive and resilient compliant strain gauges for soft machines. *Nature* **587**, 219–224 (2020).
11. Gorissen, B. et al. Elastic Inflatable Actuators for Soft Robotic Applications. *Adv. Mater.* **29**, 1604977 (2017).
12. Kim, J. et al. Stretchable silicon nanoribbon electronics for skin prosthesis. *Nat. Commun.* **5**, 5747 (2014).
13. Gong, S. et al. A wearable and highly sensitive pressure sensor with ultrathin gold nanowires. *Nat. Commun.* **5**, 3132 (2014).
14. Huang, C. B. et al. Molecule-Graphene Hybrid Materials with Tunable Mechanoresponse: Highly Sensitive Pressure Sensors for Health Monitoring. *Adv. Mater.* **31**, e1804600 (2019).
15. Bai, N. et al. Graded intrafillable architecture-based iontronic pressure sensor with ultra-broad-range high sensitivity. *Nat. Commun.* **11**, 209 (2020).
16. Ji, B. et al. Bio-Inspired Hybrid Dielectric for Capacitive and Triboelectric Tactile Sensors with High Sensitivity and Ultrawide Linearity Range. *Adv. Mater.* **33**, e2100859 (2021).
17. Wang, Z. L. & Song, J. Piezoelectric nanogenerators based on zinc oxide nanowire arrays. *Science* **312**, 242–246 (2006).
18. Shin, K.-Y., Lee, J. S. & Jang, J. Highly sensitive, wearable and wireless pressure sensor using free-standing ZnO nanoneedle/PVDF hybrid thin film for heart rate monitoring. *Nano Energy* **22**, 95–104 (2016).
19. Zhu, X. X. et al. Triboelectrification-enabled touch sensing for self-powered position mapping and dynamic tracking by a flexible and area-scalable sensor array. *Nano Energy* **41**, 387–393 (2017).
20. Zhu, G. et al. Self-powered, ultrasensitive, flexible tactile sensors based on contact electrification. *Nano Lett.* **14**, 3208–3213 (2014).
21. Liu, W. et al. Piezoresistive Pressure Sensor Based on Synergistical Innerconnect Polyvinyl Alcohol Nanowires/Wrinkled Graphene Film. *Small* **14**, e1704149 (2018).
22. Choong, C. L. et al. Highly stretchable resistive pressure sensors using a conductive elastomeric composite on a micropyramid array. *Adv. Mater.* **26**, 3451–3458 (2014).
23. Park, J. et al. Giant tunneling piezoresistance of composite elastomers with interlocked microdome arrays for ultrasensitive and multimodal electronic skins. *ACS Nano* **8**, 4689–4697 (2014).
24. Ghosh, R. et al. Fabrication of piezoresistive Si nanorod-based pressure sensor arrays: A promising candidate for portable breath monitoring devices. *Nano Energy* **80**, 105537 (2021).
25. Pang, C. et al. A flexible and highly sensitive strain-gauge sensor using reversible interlocking of nanofibres. *Nat. Mater.* **11**, 795–801 (2012).
26. Zhou, K. et al. Template-Directed Growth of Hierarchical MOF Hybrid Arrays for Tactile Sensor. *Adv. Funct. Mater.* **30**, 2001296 (2020).
27. Li, X. et al. Ultracomfortable Hierarchical Nanonetwork for Highly Sensitive Pressure Sensor. *ACS Nano* **14**, 9605–9612 (2020).
28. Yang, T. et al. Hierarchically Microstructure-Bioinspired Flexible Piezoresistive Bioelectronics. *ACS Nano* **15**, 11555–11563 (2021).
29. Kim, S. et al. Wearable, Ultrawide-Range, and Bending-Insensitive Pressure Sensor Based on Carbon Nanotube Network-Coated Porous Elastomer Sponges for Human Interface and Healthcare Devices. *ACS Appl. Mater. Interfac.* **11**, 23639–23648 (2019).
30. Lee, Y. et al. Flexible Ferroelectric Sensors with Ultrahigh Pressure Sensitivity and Linear Response over Exceptionally Broad Pressure Range. *ACS Nano* **12**, 4045–4054 (2018).
31. Turco, A. et al. An innovative, fast and facile soft-template approach for the fabrication of porous PDMS for oil–water separation. *J. Mater. Chem. A* **5**, 23785–23793 (2017).
32. Zhang, L. et al. Paraffin Oil Based Soft-Template Approach to Fabricate Reusable Porous PDMS Sponge for Effective Oil/Water Separation. *Langmuir* **35**, 11123–11131 (2019).
33. Xu, J. et al. Selective coaxial ink 3D printing for single-pass fabrication of smart elastomeric foam with embedded stretchable sensor. *Addit. Manuf.* **36**, 101487 (2020).
34. Zou, B. et al. Repurposed Leather with Sensing Capabilities for Multifunctional Electronic Skin. *Adv. Sci.* **6**, 1801283 (2019).
35. Bae, G. Y. et al. Linearly and Highly Pressure-Sensitive Electronic Skin Based on a Bioinspired Hierarchical Structural Array. *Adv. Mater.* **28**, 5300–5306 (2016).
36. Liu, M. et al. Large-Area All-Textile Pressure Sensors for Monitoring Human Motion and Physiological Signals. *Adv. Mater.* **29**, 1703700 (2017).
37. Shi, J. et al. Multiscale Hierarchical Design of a Flexible Piezoresistive Pressure Sensor with High Sensitivity and Wide Linearity Range. *Small* **14**, e1800819 (2018).
38. Guo, Y. et al. A Wearable Transient Pressure Sensor Made with MXene Nanosheets for Sensitive Broad-Range Human-Machine Interfacing. *Nano Lett.* **19**, 1143–1150 (2019).
39. Yu, T. et al. Graphene foam pressure sensor based on fractal electrode with high sensitivity and wide linear range. *Carbon* **182**, 497–505 (2021).
40. Chao, M. et al. Breathable Ti3C2Tx MXene/Protein Nanocomposites for Ultrasensitive Medical Pressure Sensor with Degradability in Solvents. *ACS Nano* **15**, 9746–9758 (2021).
41. Li, W. et al. Synergy of Porous Structure and Microstructure in Piezoresistive Material for High-Performance and Flexible Pressure Sensors. *ACS Appl. Mater. Interfac.* **13**, 19211–19220 (2021).
42. Zheng, Y. et al. Conductive MXene/cotton fabric based pressure sensor with both high sensitivity and wide sensing range for human motion detection and E-skin. *Chem. Eng. J.* **420**, 127720 (2021).
43. Wu, Q. et al. Triode-Mimicking Graphene Pressure Sensor with Positive Resistance Variation for Physiology and Motion Monitoring. *ACS Nano* **14**, 10104–10114 (2020).
44. Zhao, T. et al. Pollen-Shaped Hierarchical Structure for Pressure Sensors with High Sensitivity in an Ultrabroad Linear Response Range. *ACS Appl. Mater. Interfac.* **12**, 55362–55371 (2020).
45. Zhu, G. et al. 3D Printed Skin-Inspired Flexible Pressure Sensor with Gradient Porous Structure for Tunable High Sensitivity and Wide Linearity Range. *Adv. Mater. Technol.* **7**, 2101239 (2021).
46. Bae, K. et al. Large-Area, Crosstalk-Free, Flexible Tactile Sensor Matrix Pixelated by Mesh Layers. *ACS Appl. Mater. Interfac.* **13**, 12259–12267 (2021).
47. Yue, Z. et al. Sponge Graphene Aerogel Pressure Sensors with an Extremely Wide Operation Range for Human Recognition and Motion Detection. *ACS Appl. Electron. Mater.* **3**, 1301–1310 (2021).
48. Bai, N. et al. Graded Interlocks for Iontronic Pressure Sensors with High Sensitivity and High Linearity over a Broad Range. *ACS Nano* **16**, 4338–4347 (2022).
49. Zhang, Y. et al. Highly stable flexible pressure sensors with a quasi-homogeneous composition and interlinked interfaces. *Nat. Commun.* **13**, 1317 (2022).
50. Lee, Y. et al. Bioinspired Gradient Conductivity and Stiffness for Ultrasensitive Electronic Skins. *ACS Nano* **15**, 1795–1804 (2021).
51. Park, J. et al. Tailoring force sensitivity and selectivity by microstructure engineering of multidirectional electronic skins. *NPG Asia Mater.* **10**, 163–176 (2018).
52. Kim, Y. R. et al. Binary Spiky/Spherical Nanoparticle Films with Hierarchical Micro/Nanostructures for High-Performance Flexible Pressure Sensors. *ACS Appl. Mater. Interfac.* **12**, 58403–58411 (2020).
53. Pyo, S. et al. Multi-Layered, Hierarchical Fabric-Based Tactile Sensors with High Sensitivity and Linearity in Ultrawide Pressure Range. *Adv. Funct. Mater.* **29**, 1902484 (2019).

54. Yin, Y. M. et al. Facile Fabrication of Flexible Pressure Sensor with Programmable Lattice Structure. *ACS Appl. Mater. Interfac.* **13**, 10388–10396 (2021).

55. Nie, B. et al. Textile-Based Wireless Pressure Sensor Array for Human-Interactive Sensing. *Adv. Funct. Mater.* **29**, 1808786 (2019).

56. van Schie, C. H. A review of the biomechanics of the diabetic foot. *Int. J. Low. Extrem. Wounds* **4**, 160–170 (2005).

57. Pang, Y. et al. Epidermis Microstructure Inspired Graphene Pressure Sensor with Random Distributed Spinosum for High Sensitivity and Large Linearity. *ACS Nano* **12**, 2346–2354 (2018).

ACKNOWLEDGEMENTS

AUTHOR CONTRIBUTIONS

J.X. and H.L. contributed equally to this work. G.Z. and J.X. conceived the idea and designed the experiments. J.X., Y.Y., X.L., H.F., W.B., and H.T., carried out the device development and the performance measurement. J.X., H.L., F.X., J.C. contributed to the FEA simulation and drawing of schematic diagram. J.X., H.L., Y.Y., X.L., J.C., H.F. W.B., and H.T. participated in the discussion of the experimental data. J.X. analyzed the experimental results and wrote the paper. J.X., H.L., and Y.Y. participated in the revision of the paper. G.Z. and H.L. supervised the research process.

COMPETING INTERESTS

The authors declare no competing interests.

ADDITIONAL INFORMATION